



Spatial variability of erodibility of fine sediments deposited in gravel river beds: from field measurements to 2D numerical models

Hanna Haddad^{1,2,3} · Cédric Legout¹ · Magali Jodeau^{2,3}

Received: 17 May 2022 / Accepted: 13 January 2023 / Published online: 24 February 2023
© The Author(s), under exclusive licence to Springer-Verlag GmbH Germany, part of Springer Nature 2023

Abstract

Purpose Gravel-bed rivers can store significant amounts of fine sediments, in the gravel matrix or at the bar surface. The contribution of the latter to suspended sediment fluxes depends on their erodibility which is highly variable spatially. The sensitivity induced by this spatial variability on outputs of a 2D hydro-sedimentary numerical model was investigated and recommendations for in situ erodibility measurement strategy were provided.

Methods The spatial variability of fine sediment erodibility was determined using the Cohesive Strength Meter (CSM) device in a 1-km-long river reach of the Galabre River in the southern French Alps. A 2D hydro-sedimentary numerical model was built on the monitored reach displaying three deposit zones with distinct erodibility values. The sensitivity of the modeled eroded masses to sediment erodibility variability was assessed through ten distinct sediment erodibility settings and three schematic flood events, based on the in situ monitoring of the river.

Results and discussion The spatial variability of fine sediment deposit erodibility was significant. Marginal deposits were more resistant than superficial or water-saturated ones. The sensitivity of the modeled eroded mass to erodibility parameters was different depending on the set of measurements used. When considering the entire dataset, which exhaustively characterizes the fine sediment deposits, the numerical sensitivity was relatively low. On the other hand, when a partial set of measurements outside the quartiles was considered, the sensitivity was more significant leading to large differences in eroded masses between spatially distributed and spatially averaged settings. Using bootstrap sampling, we recommended making 15 to 20 measurements in marginal and superficial zones to adequately capture the distribution of erodibility.

Conclusions This work provided insight on the spatial variability of erodibility and the sensitivity induced in 2D numerical modeling of fine sediments. The proposed methodology could be applied to other environments (e.g., reservoirs, estuaries, or lowland rivers) in order to adapt the monitoring and numerical modeling strategies.

Keywords Erodibility · Cohesive sediment · Gravel-bed rivers · Numerical modeling · Sensitivity

1 Introduction

Suspended sediments (SS) are essential components in rivers. They represent over 90% of the total sediment flux in the river system (Syvitski et al. 2003). They are key factors in

the transport, the storage, and the redistribution of nutrients as well as contaminants at the global hydrographic scale (Walling et al. 2003; Estrany et al. 2011). It has also been established that high concentrations of fine sediments impact aquatic ecosystems as they contribute to the degradation of aquatic habitat and the alteration of fish respiratory organs (Kemp et al. 2011; Mathers et al. 2017). They are also stored in reservoirs and can induce environmental and safety issues related to dam management (Syvitski 2005; Kondolf et al. 2014). Therefore, understanding fine sediment dynamics is necessary to mitigate environmental and health issues.

Even though SS are composed of small particles with low settling velocities, evidence from previous studies showed that they undergo multiple deposition and re-entrainment phases as they are transported in the river system (Fryirs

Responsible editor: Robert Grabowski

✉ Hanna Haddad
hanna.haddad1995@gmail.com

¹ Institute of Engineering and Management Univ. Grenoble Alpes, IGE, Grenoble, France

² National Laboratory for Hydraulics and Environment (LNHE), EDF R&D, Chatou, France

³ Saint-Venant Laboratory for Hydraulics (LHSV), ENPC, EDF R&D, Chatou, France

2013; Wilkes et al. 2018). In particular, gravel-bed rivers have a high potential to store fine sediments, due to their specific morphology, bed material, and the intermittent sediment fluxes in these environments (Hodgkins et al. 2003; Orwin and Smart 2004; Navratil et al. 2010). Misset et al. (2021) and Navratil et al. (2010) also evidenced that fine sediments stored in these rivers can be of the same order of magnitude as mean annual fine sediment fluxes. This raises questions about the remobilization dynamics of these fine particles and their contribution to the SS flux.

Two types of fine sediment storages can be distinguished in gravel-bed rivers: those infiltrated in the bed matrix and those deposited at the surface of the gravels. The analysis of datasets acquired in several alpine rivers (Misset et al. 2019) as well as the application of conceptual models (Park and Hunt 2017) evidenced that the sediments stored in the bed matrix are re-mobilized when the bed itself is mobilized. They are thus stored as long as the critical bedload threshold is not exceeded, implying rather long storage periods depending on the hydrological regime of the catchment. On the other hand, fine sediments deposited at the surface of gravels are more exposed to the flow and are thus assumed to be remobilized more frequently during smaller floods without bed mobility. However, the dynamics of these deposits remains poorly studied. Thus, even though the stock of fine sediments deposited at the surface can be smaller in volume than the infiltrated one (Misset et al. 2021), its characterization is relevant to better understand SS fluxes since it is assumed to be more dynamic. Depending on the location of the river, fine sediments may include variable proportions of sand and cohesive sediments. This paper focuses on cohesive sediments (i.e., sediments with a median diameter smaller than 63 μm) deposited at the surface of gravel bars.

The re-entrainment of deposited cohesive sediments depends on the water discharges and the associated bed shear stresses during events as well as the erosion characteristics of the sediments and their spatial variability. Two essential sediment variables control their erosion in physically based numerical models: the critical erosion shear stress τ_{ce} and the erosion rate M (Partheniades 1965). Several studies have quantified these variables and their variability, mainly in estuaries and lowland rivers (Tolhurst et al. 2006; Bale et al. 2006; Lumborg et al. 2006; Widdows et al. 2007; Grabowski et al. 2012; Harris et al. 2016; Joensuu et al. 2018; Allen et al. 2021) but rarely in gravel-bed rivers (Legout et al. 2018; Haddad et al. 2022). These studies demonstrate that the spatial variability of erodibility of cohesive sediments, mainly controlled by the moisture of the deposits (Haddad et al. 2022), is significant and highlights the need to multiply measurements to assess the whole distribution of erodibility.

Physically based hydrodynamic and morphodynamic numerical models are used to better understand and predict cohesive sediment dynamics. However, they are confronted

to two main issues: (i) the lack of data on sediment erodibility variables and (ii) the sensitivity of their outputs (e.g., SS flux and eroded mass) to sediment properties. When few or no measurements are available, authors often use τ_{ce} and M values extracted from the literature (Lopes et al. 2006; Chen et al. 2021) or perform a calibration of the erodibility variables (Brand et al. 2015; Orseau et al. 2021). Therefore, in general, a unique value for each variable is assigned on the whole domain, due to the lack of distributed data (Dong et al. 2020; Feng et al. 2020). As some studies showed that model outputs depend on particle properties (Chou et al. 2018; Dong et al. 2020), this highlights the need to assess the impact of the choices made during the erodibility parametrization on model outputs. To the authors' knowledge, no study has quantified the sensitivity of physically based model outputs to the spatial variability of erodibility. We therefore investigated this issue in a gravel-bed river that was extensively characterized with in situ erodibility measurements performed on cohesive sediment deposits.

The aim of this work was to assess the sensitivity of modeled eroded mass to the spatial variability of the erodibility of cohesive deposited sediments. The purpose was also to establish if the spatial variability of the erodibility of cohesive sediments should be considered in bi-dimensional numerical models or if a unique averaged value was sufficient to correctly model the amount of cohesive sediments eroded from the river bed. The first step was to reanalyze in situ erodibility data presented in Haddad et al. (2022) in order to define several settings as inputs for a 2D hydrodynamic and sediment model of a 1 km river reach. After checking that the model reproduced the flows correctly, the second step was to explore how the modeled eroded masses depend on erodibility parameter variations. Finally, recommendations were proposed to optimize the field measurement strategy considering the numerical sensitivity results.

2 Material and methods

2.1 Study site

A 1 km reach of an Alpine gravel-bed river was considered in this study. The Galabre River is located in the southern French Alps. It is part of the Draix-Bléone research observatory and the French network of critical zone observatories (OZCAR; Gaillardet et al. 2018). Discharge and suspended sediment concentrations (SSC) time series are available since 2007 at the upstream gauging station (draining 20 km²) and since 2018 at the downstream gauging station (draining 35 km²). The stations are 2.5 km apart. The catchment description, the equipment, and the dataset collected at the upstream station are presented in Legout et al. (2021), while the downstream station ("Riple") is presented in Nord et al.

(2020). The mean annual water discharge and suspended sediment yield recorded at the upstream station are $0.281 \text{ m}^3 \text{ s}^{-1}$ and $670 \text{ t km}^{-2} \text{ year}^{-1}$, respectively. High amounts of cohesive sediments, originating from badlands developed in marl and molasse lithologies, are transported during short periods (50% of the total flux in 0.1% of the time; Navratil et al. 2011). SSC reach more than 100 g L^{-1} , particularly during spring and summer events (Esteves et al. 2019). The average bed slope of the 1 km long study reach located upstream the downstream station is 2%. The river width ranges from 5 to 10 m. The riverbed is braided with vegetated bars and banks that can be submerged for discharges higher than $10 \text{ m}^3 \text{ s}^{-1}$. Cohesive sediments are present inside the gravel bed (median diameter $d_{50} = 3.5 \text{ cm}$) and at the surface of the gravel bars. During the summer floods that can be highly concentrated in suspended sediments (between 10 and 100 g L^{-1}) and with low flows (between 1 and $5 \text{ m}^3 \text{ s}^{-1}$; Esteves et al. 2019), a significant amount of cohesive sediments is likely to be deposited at the surface of the gravel bed, thus replenishing the stock of cohesive material. Cohesive sediments deposited at the surface of gravel bars are composed of black marl and molasse deposits. Both show cohesive properties due to their grain size smaller than $63 \mu\text{m}$ (Haddad et al. 2022).

2.2 Delimitation of the deposit zones

Multiple methods were combined to identify and classify different zones of cohesive sediment deposits during the field campaign conducted by Haddad et al. (2022) in August 2019: (i) visual identification of the deposits, (ii) measurements of the volumetric water content (%) using a delta-T SM150 probe, and (iii) measurements of the heights of the deposits from water level using a dGPS. Following the deposit typologies of Wood and Armitage (1999) and Camenen et al. (2013), the three following deposits were found in the Galabre River at the surface of gravel bars (Fig. 1):

- (i) Water-saturated deposits, in the areas regularly flooded during very low floods, resulting in the deposition of cohesive sediments in wet areas;
- (ii) Marginal deposits, i.e., deposits close to the flow and frequently underwater in the area inundated by low floods;
- (iii) Superficial deposits, i.e., cohesive sediments at the top of gravel bars, deposited during floods that submerged bars.

A fourth zone was defined as the talweg area submerged at low flow where hydraulic shear stresses are often high and do not allow deposition of cohesive material.

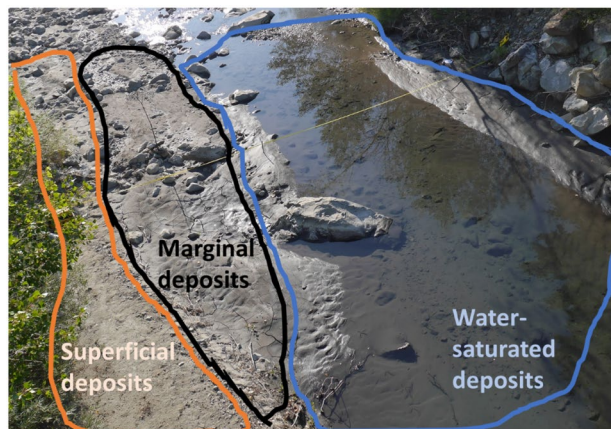


Fig. 1 Zones of cohesive sediment deposits (superficial, marginal, and water-saturated zones), picture taken August 27th, 2019

2.3 Hydro- and morphodynamic numerical modeling

Hydrodynamics and cohesive sediment transport are computed with the open source Telemac-Mascaret Modeling System. Hydraulics are computed by solving the 2D shallow-water equations (Hervouet 2007). A module for sediment transport (GAIA) is coupled internally at each time step (Audouin et al. 2020; Tassi et al. 2023). In this study, we consider only cohesive sediments transported as suspended load. Sediments are transported with an advection–dispersion equation, and the deposit and erosion fluxes are calculated using the following Partheniades (1965) and Krone (1962) equations:

$$E = \begin{cases} M \left[\left(\frac{\tau_b}{\tau_{ce}} \right) - 1 \right] & \text{if } \tau_b > \tau_{ce} \\ 0 & \text{otherwise} \end{cases} \quad (1)$$

$$D = \begin{cases} w_s \cdot C \left(1 - \frac{\tau_b}{\tau_{cd}} \right) & \text{if } \tau_b < \tau_{cd} \\ 0 & \text{otherwise} \end{cases} \quad (2)$$

where E ($\text{kg m}^{-2} \text{ s}^{-1}$) is the erosion flux, τ_b (N m^{-2}) is the bottom shear stress, τ_{ce} (N m^{-2}) is the critical shear stress, M ($\text{kg m}^{-2} \text{ s}^{-1}$) is the Partheniades erosion rate constant, D ($\text{kg m}^{-2} \text{ s}^{-1}$) is the deposit flux, w_s (m s^{-1}) is the settling velocity of the cohesive sediment, C (kg L^{-1}) is the depth-averaged concentration, and τ_{cd} (N m^{-2}) is the critical shear stress for sediment deposition.

The bed evolution is calculated with the Exner mass-balance equation:

$$\rho(1 - \lambda) \frac{\partial z_b}{\partial t} = D - E \quad (3)$$

where ρ (1650 kg m^{-3}) is the sediment density, λ (-) is the bed porosity, and z_b (m) is the bed level.

The model domain consisted of a 1-km-long reach of the Galabre River upstream the “Riple” hydro-sedimentary station (Fig. 2).

The digital elevation model (DEM) of the riverbed (Fig. 2) was based on the high-resolution topography dataset acquired in the summer and autumn 2019: dGPS measurements (28/08/2019), airborne Lidar data (25/10/2018), and photogrammetric data from a drone flight (06/09/2019). The talweg riverbed was built with the photogrammetric data (accuracy approx. ± 10 cm). On the banks, the Lidar data were used where the photogrammetric data were missing. In the vegetated areas, where the Lidar data were erroneous, the topography was interpolated using the nearest unvegetated data. The density of this resulting DEM is 200 points/m².

To allow flow stabilization and to avoid backwater effects, the mesh was extended in the upstream and downstream directions with a flat bed of 10 m width and 2 % slope. The liquid discharges were set at the upstream boundary condition. At the downstream condition, the water height was set depending on the discharge and following the Manning–Strickler formula. The downstream sediment conditions were set as free.

The computational domain was discretized with triangular elements with a resolution of 0.5 m. The computational time step was set at $\Delta t = 0.1$ s to keep the Courant number around 1. Mesh sensitivity analysis was conducted to make sure the chosen mesh captured the local flow recirculations that drive the sedimentary processes (see Appendix A).

The friction was simulated with a Strickler law and a uniform coefficient $K = 25 \text{ m}^{1/3} \text{ s}^{-1}$. This value generated the lowest difference between the field measurements and the numerical results, except for one dataset (flood water levels) for which the measurements were the most uncertain (see Appendix B).

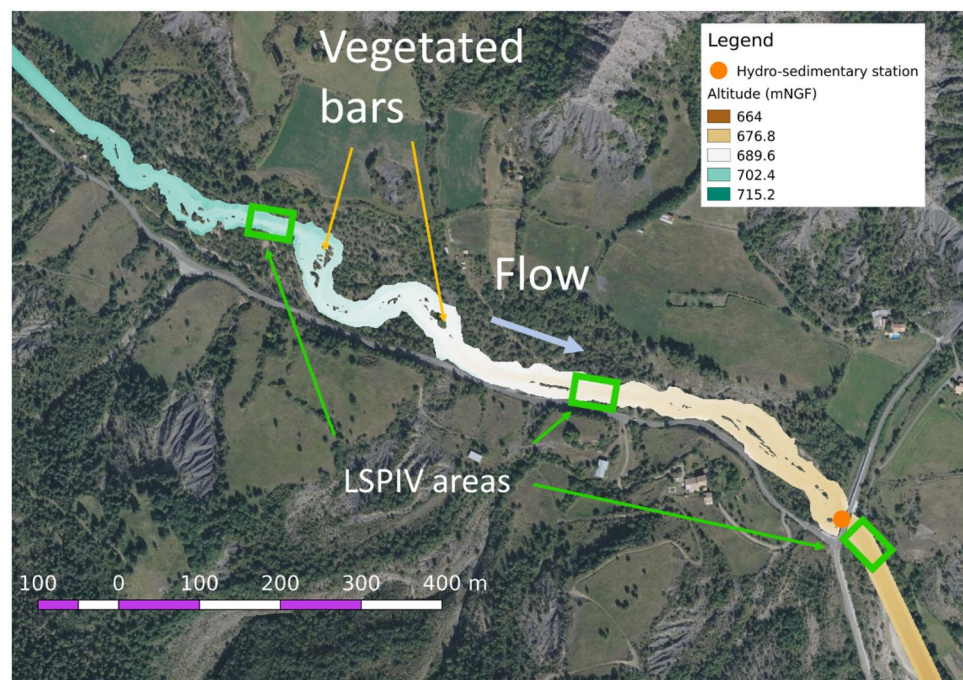
The riverbed composed of pebbles ($d_{50} = 3.5$ cm, $d_{90} = 10$ cm) was assumed to be stable. For most scenarios and deposits, the simulated discharges were lower than the inception of motion of these particles, estimated with the Shields curve around $5 \text{ m}^3 \text{ s}^{-1}$. In this numerical model, only cohesive sediments can be eroded, transported, and deposited at the top of the gravel bed (surface deposits). Deposition and erosion of cohesive sediments within the pores of gravels are not represented in this model.

2.4 Cohesive sediment numerical parameters and simulated scenarios

2.4.1 Hydraulic scenarios

Three hydraulic scenarios were used to assess the numerical model’s sensitivity to erosion properties of cohesive sediments (Fig. 3). To simplify the analysis, triangular hydrographs were constructed for the scenarios. “Er1” was based on the actual flood that occurred in the Galabre River on 22/09/2019 and was representative of end of summer events with discharges occurring several times a year. The peak discharge during the flood was $Q_{\text{max,Er1}} = 1.6$

Fig. 2 Digital elevation model on the Galabre reach. The hydraulic model was evaluated with surface velocities of the flow measured by Large Scale Particle Image Velocimetry (LSPIV) at three locations



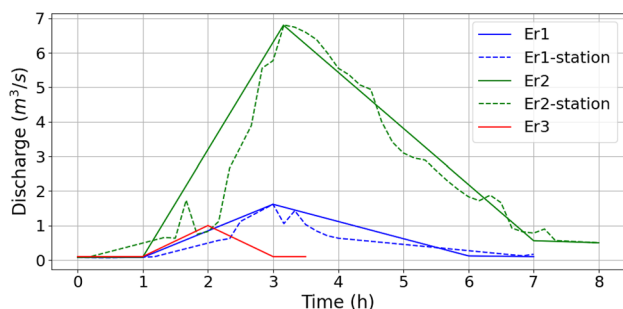


Fig. 3 Discharges during the schematic modeled events Er1, Er2, and Er3. Er1 and Er2 were based on the discharges measured at the upstream station (dotted lines)

$\text{m}^3 \text{s}^{-1}$ and the flood lasted approximately 5 h. “Er2” was based on the event that took place on 15/10/19 which was an autumnal flood with rather high discharges. The peak discharge was $Q_{\max, \text{Er}2} = 6.8 \text{ m}^3 \text{ s}^{-1}$ and the flood lasted approximately 6 h. Even though the peak discharge of “Er2” exceeds the estimated critical discharge for gravel mobility, this flood was considered as a test case representing the highest discharges in the sensitivity analysis. Indeed, the critical discharge of $5 \text{ m}^3 \text{ s}^{-1}$ is only an estimation, and even though there might be some gravel mobility during this event, the bedload would only affect the areas of the section with the highest water height and flow velocity. This would not change the process involved with the erosion of fine sediments stored at the surface of bars. The last modeled event, “Er3”, was built to investigate the sensitivity during a small flood of 2 h with a peak discharge of $Q_{\max, \text{Er}3} = 1 \text{ m}^3 \text{ s}^{-1}$ (i.e., small flood that could occur during summer in the Galabre River).

2.4.2 Cohesive sediment erodibility settings

Critical shear stress and erosion rates of the deposits were quantified in the field using the Cohesive Strength Meter (CSM, MK4, Partrak). One hundred twelve measurements were conducted in August 2019 in the three deposit zones (27 in the superficial zone, 53 in the marginal zone, and 32 in the water-saturated zone) and are presented in Haddad et al. (2022).

A brief description of the CSM test is given hereafter but the reader is referred to Haddad et al. (2022) for a more detailed description. The CSM test is based on successive vertical water jets impacting the sediment bed and inducing sediment erosion with increasing pressure. The data monitored during the test is the vertical jet pressure (kPa) and the optical transmission (%).

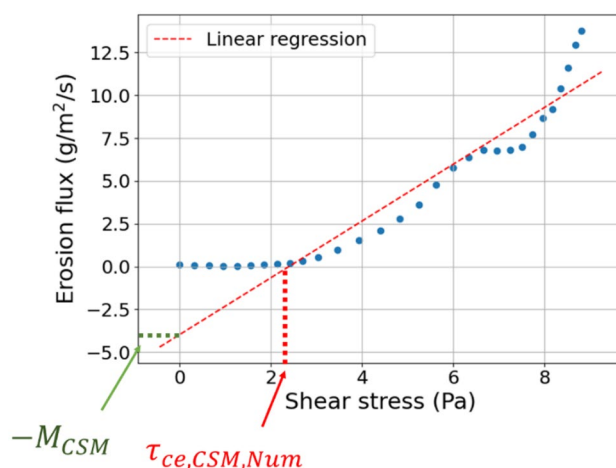


Fig. 4 Example of a signal obtained from a CSM erosion measurement: erosion flux ($\text{gm}^{-2}\text{s}^{-1}$) plotted against shear stress. τ_{ce} refers to the critical shear stress and M refers to the Partheniades constant

For each test, the raw CSM vertical jet pressures (kPa) were converted to equivalent horizontal shear stress (Pa) using the calibration of Tolhurst et al. (1999) to be used in the numerical model. The transmission (%) in the CSM chamber was converted to SSC (g L^{-1}) using a laboratory calibration from sediments sampled during the field campaign.

The mean erosion flux was calculated for each pressure step and was plotted as a function of the applied horizontal shear stress (Fig. 4). The Partheniades law (1) gives a relationship between the erosion flux and the shear stress which allows to obtain the critical shear stress ($\tau_{ce, \text{CSM}, \text{Num}}$) and the Partheniades constant (M_{CSM}) from a regression of the increasing part of the curve.

From these measurements, ten sediment erodibility settings were defined to evaluate the model output’s sensitivity to the variability of erodibility parameters. The settings were divided in two categories: spatially distributed (SDist) and spatially averaged (SAv). In the SDist settings, the three deposit zones (superficial, marginal, and water-saturated) had their own settings of both erodibility parameters τ_{ce} and M . In the SAv settings, a constant value for both erodibility parameters (τ_{ce} and M) was used on the whole domain, obtained by averaging the erodibility variables and weighting by the surface of each zone. For both the SDist and SAv settings, five sets of the variables τ_{ce} and M were defined: “Very Low Erodibility” (VLE) as minimal erodibility (excluding outliers), “Low Erodibility” (LE) as 1st quartile, “Median Erodibility” (ME) with median variables, “High Erodibility” (HE) as the 3rd quartile, and “Very High Erodibility” (VHE) with maximal erodibility (excluding outliers).

2.5 Model evaluation

The three hydraulics scenarios and the ten erodibility settings led to thirty numerical outputs. In particular, the total eroded mass in the reach at the end of the simulation and the eroded masses in the three specific zones (superficial, marginal, water-saturated) were calculated.

Two indicators on the differences in eroded masses between the erodibility settings were defined:

- The interquartile difference is the difference in eroded mass between the “HE” and the “LE” settings: $\varepsilon_{IQ,SDist} = M_{SDistHE} - M_{SDistLE}$ and $\varepsilon_{IQ,SAV} = M_{SAVHE} - M_{SAVLE}$ where ε_{IQ} is the interquartile difference on the eroded mass and M_X is the eroded mass for the setting X. This indicator corresponds to the sensitivity of the numerical model’s outputs in the case of a robust assessment of erosion properties (i.e., a large set of measurements is available defining a reliable statistical distribution). In this case, variables between the 1st and 3rd quartiles are chosen.
- The total difference is the difference in eroded mass between the settings “VHE” and “VLE”: $\varepsilon_{tot,SDist} = M_{SDistVHE} - M_{SDistVLE}$ et $\varepsilon_{tot,SAV} = M_{SAVHE} - M_{SAVLE}$ where ε_{tot} is the total difference on the eroded mass. This indicator corresponds to the sensitivity of the outputs in the case when very few field measurements are available (variables included in the whole distribution).

2.6 Sub-sampling methodology

When dealing with in situ measurements, to save monitoring time, it is needed to define the minimal sample size that correctly assesses the distribution of both erodibility parameters ($\tau_{ce,CSM,Num}$ and M_{CSM}). The following sub-sampling bootstrap methodology is applied for samples ranging from 10 to 100% of the total sample (with steps of 10%):

1. N values are randomly sampled;
2. The median, 1st, and 3rd quartiles of this sample distribution are evaluated;
3. The steps 1 and 2 are repeated 100 times;
4. The mean and standard deviation of the 100 statistics (median and quartiles) are obtained.

For each sub-sample, an estimate of the statistic (average median and quartiles) as well as an associated uncertainty (standard deviation of the statistics) are thus obtained. We consider that the statistic is correctly estimated by the sub-sample when it is in the range of $\pm 10\%$ the reference value (statistic of the total sample) and when the standard deviation of the statistic is less than 10%.

3 Results and discussion

3.1 Deposit characteristics and eroded masses in the numerical model

3.1.1 Erodibility settings

Field measurements from Haddad et al. (2022) were re-analyzed to configure the erodibility settings of the numerical model. Figure 5a shows that the moisture of cohesive deposits was well correlated with their height above water level. It enables to define the location of the three deposit zones according to their relative heights from the flow level. The water-saturated deposits (> 50% moisture) had a height $z < 5$ cm above water level while the superficial deposits (< 15% moisture) had a height $z > 25$ cm above water level. The marginal deposits were located in an intermediate position and were characterized by water contents between 15 and 50%. The thickness of the deposits was of the same order of magnitude (about 5 cm on average) in each zone (Fig. 5b). Figure 5c, d show that the erodibility variables exhibited both variations between and within deposit zones. Concerning the critical shear stress for erosion τ_{ce} , the deposits in the marginal zones exhibited the highest variability but were also the most resistant. The differences between deposit zones were less pronounced for the Partheniades constant M . As this organization of deposits erodibility was also observed in another mountain river (i.e., Isère River) presented in Haddad et al. (2022), we assumed it could be a common characteristic of gravel-bed rivers due to their morphology. The distribution of the calibrated erodibility parameters (τ_{ce} and M) obtained from the CSM measurements (Fig. 5c, d) allowed to define the values of the spatially distributed and spatially averaged settings (Table 1).

3.1.2 Spatial extension of deposits in the initial state

The location of the deposits that were measured during the field campaign in late August 2019 was related to the preceding floods. Two kinds of hydro-sedimentary events occurred in July and August 2019. Medium and high floods (July 1st, 15th, and 27th) with discharges between 1 and 4.5 m³·s⁻¹ and SSC between 40 and 200 g L⁻¹, supplied sediments in the marginal and superficial areas. The 24th August event with low discharge (max 0.1 m³ s⁻¹) and max SSC of 30 g L⁻¹ supplied cohesive sediments in the water-saturated and marginal zones. These events are presented in detail in Haddad et al. (2022). Nevertheless, it was not possible to define in the numerical model each of the four deposit zones (talweg, water-saturated,

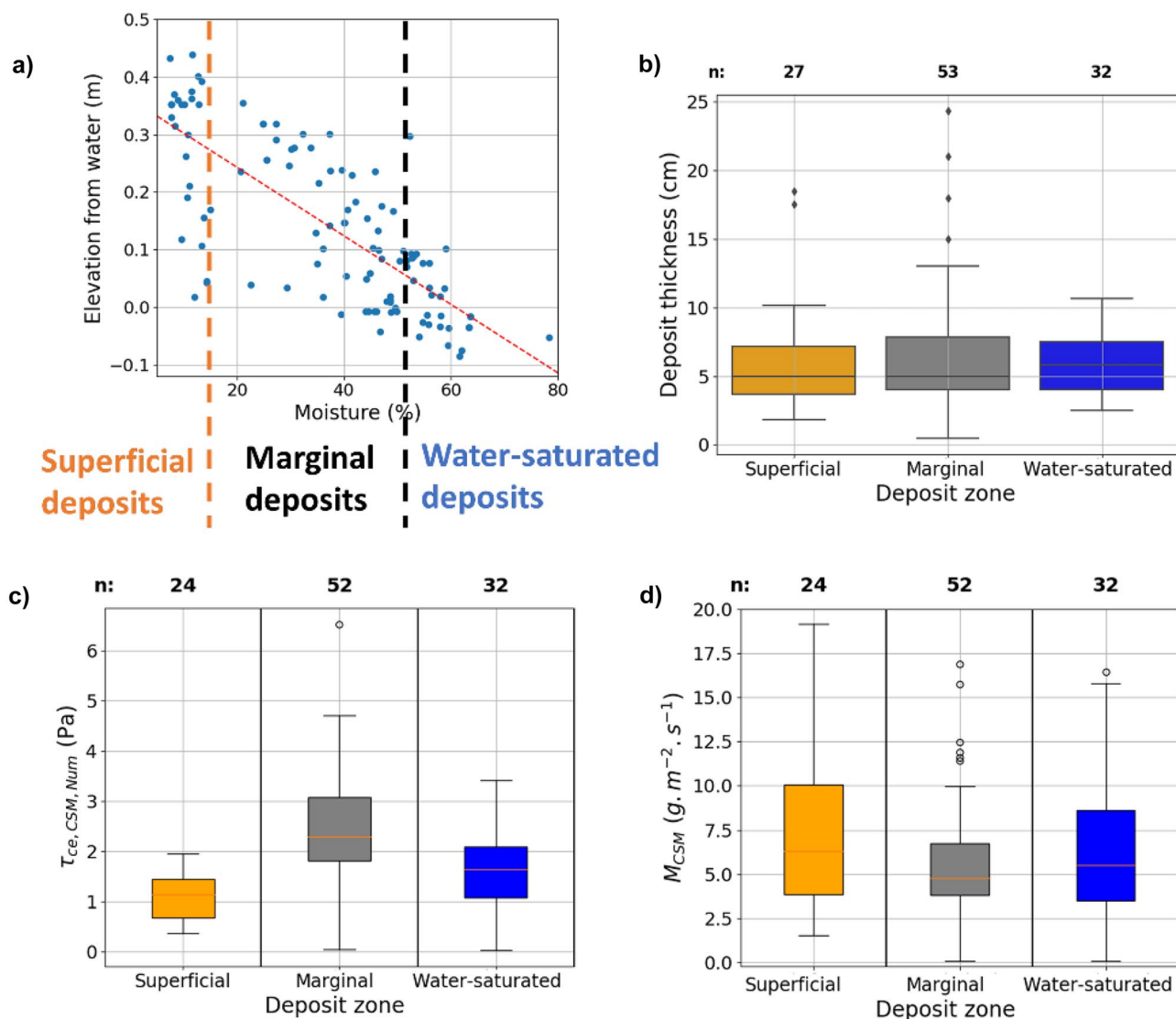


Fig. 5 Characteristics of the measurements during the August 2019 campaign on the Galabre River: **a** relative height of the deposit zones above the free surface as a function of bulk moisture, **b** deposit thickness, **c** critical shear stresses, and **d** Partheniades con-

stants obtained from the CSM measurements in each zone. n corresponds to the number of measurements made in the three deposit zones (water-saturated, marginal, and superficial)

marginal, and superficial) as visually observed due to the uncertainties of the digital elevation model and the simplifications made during the mesh generation. Thus, in order to define realistic zones in the numerical model, flooding maps were calculated for various discharges.

To define the ranges of discharges associated with these four submerged zones, an analysis of the summer floods of the Galabre River over the period 2007–2019 was performed (Fig. 6a, b). According to the discharge distribution during the 3 months of low flows (July, August, and September), a discharge of $Q = 0.05 \text{ m}^3 \text{ s}^{-1}$ was defined as the upper limit for the talweg area (Fig. 6a). The regularly flooded area corresponding to water-saturated deposits was defined in the

range $0.05 < Q < 0.1 \text{ m}^3 \text{ s}^{-1}$. The upper limit corresponded to the average flow during the August 2019 measurement campaign. The area of marginal deposits, inundated by summer floods, was defined for discharges between 0.1 and $1 \text{ m}^3 \text{ s}^{-1}$ (Fig. 6b). The value of $1 \text{ m}^3 \text{ s}^{-1}$ corresponded to the average of the highest floods observed during the summer. Finally, zones of superficial deposits were defined in the areas inundated for discharges varying between 1 and $5 \text{ m}^3 \text{ s}^{-1}$ (Fig. 6b). Above $5 \text{ m}^3 \text{ s}^{-1}$, flows can be morphogenic and the gravel mobility may also involve the erosion of cohesive bed matrix sediments.

Steady-state hydrodynamic simulations were performed for the four identified threshold discharges (0.05, 0.1, 1,

Table 1 Spatially distributed and spatially averaged erodibility variables, critical shear stress τ_{ce} expressed in Pa (Nm^{-2}) and Partheniades constant M expressed in gm^2s^{-1} for the different settings: “Very Low Erodibility” (VLE), “Low Erodibility” (LE), “Median Erodibility” (ME), “High Erodibility” (HE), and “Very High Erodibility” (VHE)

	τ_{ce}		M		τ_{ce}		M		τ_{ce}		M	
	SDistVLE	SDistLE	SDistME	SDistHE	SDistVHE	SAVLE	SAVME	SAVHE	SAVLE	SAVME	SAVHE	
Spatially distributed settings												
Superficial zone	1.9	1.5	3.8	1.1	6.3	0.6	10.1	0.4	20			
Marginal zone	4.8	0.09	3.8	2.3	4.7	1.8	6.7	0.04	10			
Water-saturated zone	3.4	0.1	3.5	1.6	5.5	1.1	8.6	0.03	16			
Non-spatialized settings	SAVLE	SAVLE	SAVME	SAVME	SAVHE	SAVHE	SAVHE	SAVHE				
All deposits	3.2	0.8	3.8	1.6	5.5	1.1	8.6	0.2	15.6			

and $5\text{ m}^3\text{ s}^{-1}$) to obtain the spatial boundaries of the four zones (Fig. 7). The modeled areas of each deposit zone were 4960, 4077, and 893 m^2 for the superficial, marginal, and water-saturated zones, respectively. These zones were consistent with the ones identified in the field during the in situ monitoring campaign, with relative differences in elevations defining the different zones lower than 15% between the zones defined in the numerical model and those observed on the field. In each of these zones, a uniform layer of 5 cm was applied as initial state according to the measured thickness of the deposits (Fig. 5b).

3.1.3 Eroded masses

The total suspended sediment load during the two floods that occurred after the field campaign in August 2019 was calculated from the monitored sediment concentration and discharge at the upstream gauging station. The total load was 922 t for the first event (“Er1”) and 2134 t for the second (“Er2”). The modeled eroded masses obtained with the median scenarios were 200 t during the “Er1” event while it was 500 t during the “Er2” event (Fig. 8). Thus, the potentially re-mobilized stock from the 1 km studied reach represented more than 20% of the total load.

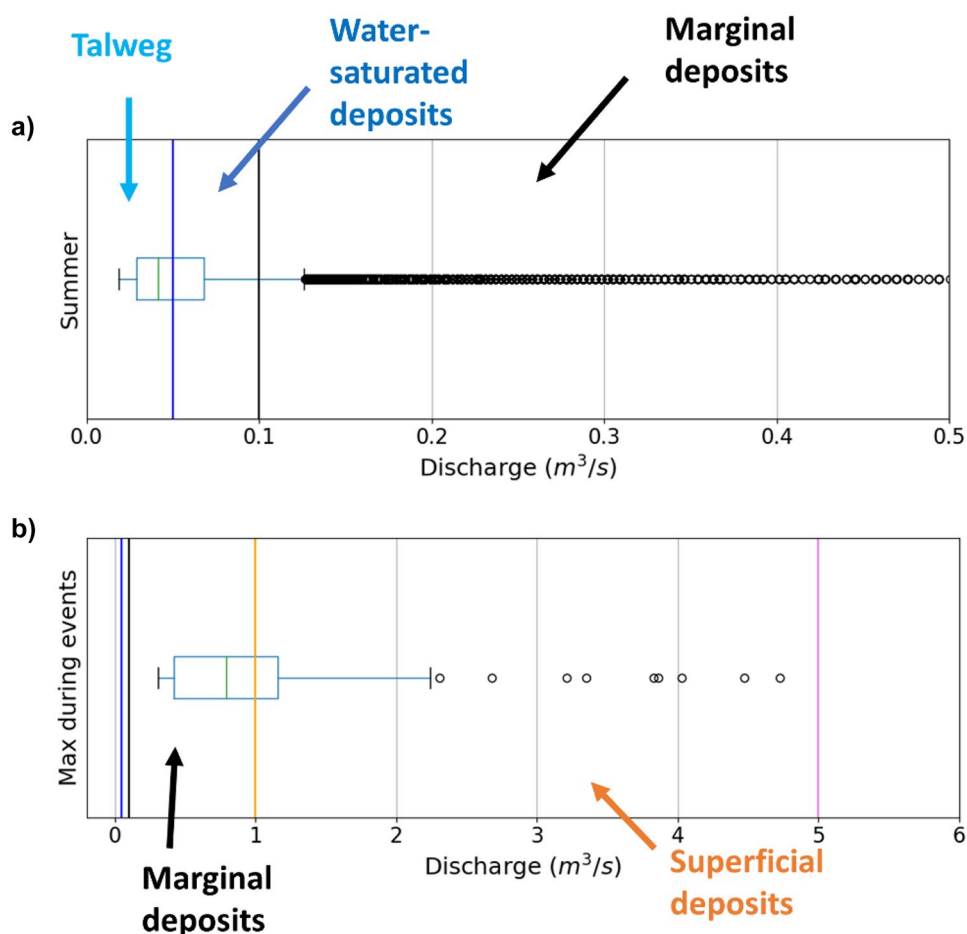
3.2 Sensitivity of modeled eroded masses to the spatial variability of erodibility measurements

3.2.1 Effect on the total eroded mass in the modeled river reach

The main objective of the numerical analysis performed with different erodibility settings was not to assess which scenario (spatially distributed or averaged) better represents the reality, but rather to investigate if the spatial variation of erodibility within the three deposit zones had a significant effect on the total modeled eroded mass.

Assuming that the dataset acquired in August 2019 was representative of the distribution of the spatial variability of the erodibility in each zone, a first sensitivity analysis was conducted within the range of erodibility parameters equal to the 1st, 2nd, and 3rd quartiles of the measurements shown in Fig. 5c, d. These refer to the three erodibility settings SDistLE, SDistME, and SDistHE in Fig. 8. For the three schematic floods, the interquartile differences (differences in eroded masses between SDistLE and SDistHE, $\epsilon_{IQ,SDist}$) ranged from 18% (for Er2) to 60% (for Er3) of the total eroded mass modeled for the median scenarios (Table 2). These deviations suggest that the intra-zone spatial variability of erodibility had a low impact on the total eroded modeled masses.

Fig. 6 **a** Distribution of Galabre River flows during summer (July, August, and September) and **b** distribution of maximum flows reached during summer floods (total of 56 summer events over the period 2007–2019). The labels talweg, water-saturated deposits, marginal deposits, and superficial deposits refer to the zones that are inundated at that discharge



This moderate sensitivity to intra-zone spatial variability obtained by considering distinct settings in the three deposition zones raised the question of the sensitivity of the total modeled masses to inter-zone spatial variability. As in most numerical models, the erodibility parameters do not vary in space, one may therefore wonder what the differences between spatially averaged or distributed settings for erodibility could be. The results of the three previous spatially distributed settings (i.e., SDistLE, SDistME, and SDistHE) were thus compared to the spatially averaged ones: SAVLE, SAVME, and SAVHE. For the small floods (i.e., Er1 and Er3), the eroded masses of the spatially distributed settings were slightly lower (relative difference of approx. 14% for scenario Er1 and median setting) than those of the spatially averaged settings (Fig. 8 and Table 2). On the contrary, higher floods, like Er2, generated slightly higher eroded masses (relative difference of approx. 3% for scenario Er2 and median setting) with the spatially distributed settings than with the spatially averaged settings. But in general terms, the total eroded mass exhibited very small differences between SDist and SAV settings for all the schematic events (comparison between blue and red bars in Fig. 8). This means that if the objective of numerical modeling is to

obtain a correct estimate of the total eroded mass in the river reach, without being interested in the contribution of each deposit zone, it does not seem essential to assign specific values according to the deposition zones. An average value on the whole reach leads to the same results.

This first conclusion relating to the small differences between SDist and SAV settings is however valid if the measurement set allows a robust estimation of the mean value and the interquartile range. When very few measurements are available, the spatial variability of the erodibility might not be completely assessed. Thus, the τ_{ce} and M values used to parametrize the model could be extreme values of the whole distribution. This case is evaluated comparing the scenarios where the erodibility could be highly overestimated (SDistVHE and SAVVHE) or highly underestimated (SDistVLE and SAVVLE). In these cases, the differences of total eroded masses between the SDist and SAV settings became pronounced, particularly for the least erosive settings, SDistVLE and SAVVLE (Fig. 8). As an example, during the Er2 event, the total eroded mass with the SDistVLE scenario is $M_{SDistVLE,Er2} = 148$ t and the total eroded mass with the SAVVLE scenario is $M_{SAVVLE,Er2} = 305$ t. There is a factor of 2 between both scenarios. The spatially distributed

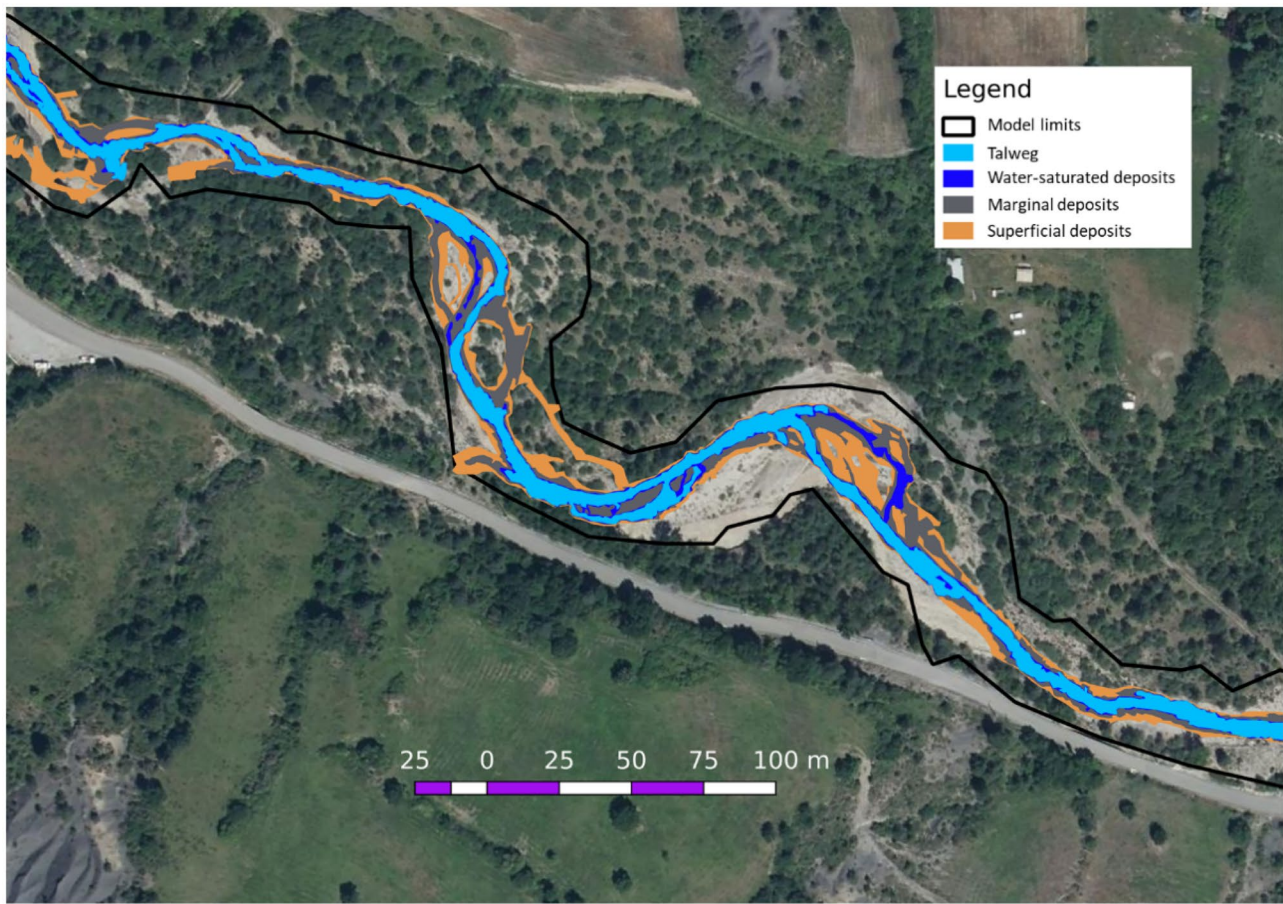


Fig. 7 Initial state of the bed, spatial extensions of the deposits zones: no sediment (talweg), water-saturated deposit zone, marginal deposit zone, and superficial deposit zone. These extensions were obtained

scenarios strongly underestimated the total eroded mass compared to the spatially averaged scenarios. These differences were reflected in the variability of the modeled total eroded masses: for all hydraulic scenarios, the total difference ϵ_{tot} was greater for the SDist than for the SAV settings (Table 2). For example, for the Er1 flood, the total difference was $\epsilon_{\text{tot,SAV,Er1}} = 249$ t for the spatially averaged settings and $\epsilon_{\text{tot,SDist,Er1}} = 315$ t for the spatially distributed settings (Table 2). This corresponds to a relative difference of 26% between both settings. For the Er2 flood, the total difference was $\epsilon_{\text{tot,SAV,Er2}} = 334$ t for the spatially averaged settings and $\epsilon_{\text{tot,SDist,Er2}} = 476$ t for the spatially distributed settings (Table 2). This corresponds to a relative difference of 43% between both settings. Thus, when available measurements do not adequately capture the distribution of the spatial variability of erodibility, using a spatial distribution of erodibility variables across the domain could lead to larger errors than using a single average value, especially for events with high peak discharges. Therefore, imposing

from numerical simulations with the discharges separating these different zones identified from Fig. 6

an average value could smooth the differences between the different areas.

3.2.2 Effect on the modeled eroded mass in each deposit zone

Since the deposit zones (superficial, marginal, and water-saturated) have contrasted erodibility (Fig. 5c, d), differences in simulated eroded masses between the settings may occur in each zone. Figure 9 shows that the marginal zone contributed the most to the total eroded mass for the three schematic events tested, for both the SDist and SAV settings. The second most contributions were from the water-saturated zone for small floods (Er1 and Er3 in Fig. 9a, b, e, f) and from the superficial zone for high floods (Er2 in Fig. 9c, d). Even though for all scenarios the eroded mass per square meter was larger for the water-saturated zone (due to its small area of 893 m^2), the total eroded mass was more important in the marginal zone (Table 3). Two properties of the marginal zone explain why it was the most contributing zone to the

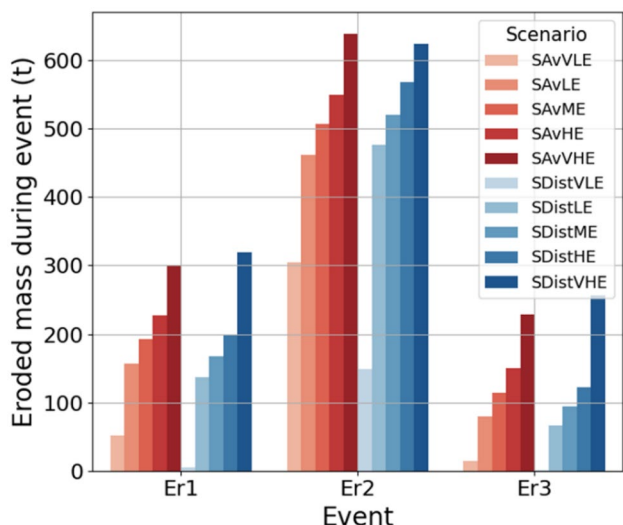


Fig. 8 Total eroded mass (t) for each of the spatially distributed and spatially averaged scenarios during the events Er1, Er2, and Er3

SS flux: the amount of cohesive sediments stored in the zone and its location. This category of deposits represented indeed a significant percentage of the deposits (41%). Even though the superficial zone contained a higher stock (50%), a larger part of the marginal zone was eroded due to the spatial configuration of these areas. The location of the marginal zone is neither too close to the flow where the shears were quickly very high nor too far from the flow in areas that were not very submersible. This makes it a zone that was more often inundated and partly remobilized during floods. The superficial zone, on the other hand, was only submerged during a limited period of the simulated hydrograph, when the flows were high enough. As a result, more erosion was observed in the marginal zone.

In contrast to the results concerning total eroded mass, the differences between SDist and SAV settings became larger when comparing the eroded mass in each zone (Fig. 9). The mass eroded in the marginal areas was lower when erosion variables were spatially distributed than when a single value was used across the domain (Fig. 9, differences between zones colored in gray between the left and right graphs). These differences were accentuated when the peak flood discharge was relatively low. As an example, for the Er1 scenario, the eroded mass in the marginal zone with the SDistME scenario was $M_{SDistME,marg,Er1} = 124$ t while

it was $M_{NSAvME,marg,Er1} = 149$ t with the SAVME scenario (Table 3). This corresponds to a relative difference of 20%. For the superficial deposits, an opposite trend was observed compared to the marginal deposits. When superficial zones were submerged, the eroded masses were larger when erosion was spatially distributed than when a single erodibility value was used (Fig. 9c, d). This trend was well illustrated through the Er2 flood for which the eroded mass in the superficial zone with the SDistME scenario was $M_{SDistME,surf,Er2} = 193$ t while it was $M_{SAvME,surf,Er2} = 172$ t with the SAVME scenario (Table 3), corresponding to a relative difference of 15%.

In conclusion, there were small differences in eroded mass between the SDist and SAV settings within the marginal and superficial areas. The eroded mass was underestimated (by about 20%) in the marginal zone and overestimated (by about 15%) in the superficial zone with a spatially distributed setting compared to a spatially averaged one. Thus, if the objective of the modeling is to precisely reproduce the evolution of the deposits in each zone and to evaluate their respective contributions to the SS flux, it seems relevant to consider the inter-zone variability in the parameterization of the models.

However, as for the sensitivity analysis performed on the modeled total eroded mass (Section 3.2.1), this conclusion is valid if the available measurement set allows a robust estimation of the quartiles of the erodibility in each zone. If the τ_{ce} and M values used to parametrize the model correspond to extreme values, larger differences can be observed. For the most erosive settings (SDistVHE and SAVVHE), little differences were obtained between SDist and SAV settings for the three zones and the three floods (Fig. 9). The main differences appeared between the SDistVLE and SAVVLE scenarios, in the marginal zone (Fig. 9). Indeed, for the Er1 scenario for example, the eroded mass was almost null in the marginal zone for the SDistVLE scenario whereas it was equal to $M_{SAvVLE,marg,Er1} = 42$ t for the SAVVLE scenario. For the Er2 flood, the eroded mass was $M_{SDistVLE,marg,Er2} = 40$ t for the SDistVLE scenario and $M_{SAvVLE,marg,Er2} = 200$ t for the SAVVLE scenario. This corresponded to a difference of 160 t while it was 50 t in the superficial area.

These results suggest that when the dataset is incomplete, the differences between the SDist and SAV settings were more significant over the different deposit zones. While the differences were moderate (around 15 to 20%) for a

Table 2 Total eroded mass for the median scenario (SDistME and SAVME), interquartile, and total difference for the three schematic floods

Hydraulic scenario ($m^3 s^{-1}$)	$M_{SDistME}$ (t)	$\epsilon_{IQ,SDist}$ (t) $\left(100 \frac{\epsilon_{IQ,SDist}}{M_{SDistME}}\right)$	$\epsilon_{tot,SDist}$ (t)	M_{SAvME} (t)	$\epsilon_{IQ,SAv}$ (t) $\left(100 \frac{\epsilon_{IQ,SAv}}{M_{SAvME}}\right)$	$\epsilon_{tot,SAv}$ (t)
Er1	168	62 (37%)	315	193	71 (37%)	249
Er2	520	92 (18%)	476	506	87 (17%)	334
Er3	94	56 (60%)	255	114	71 (62%)	214

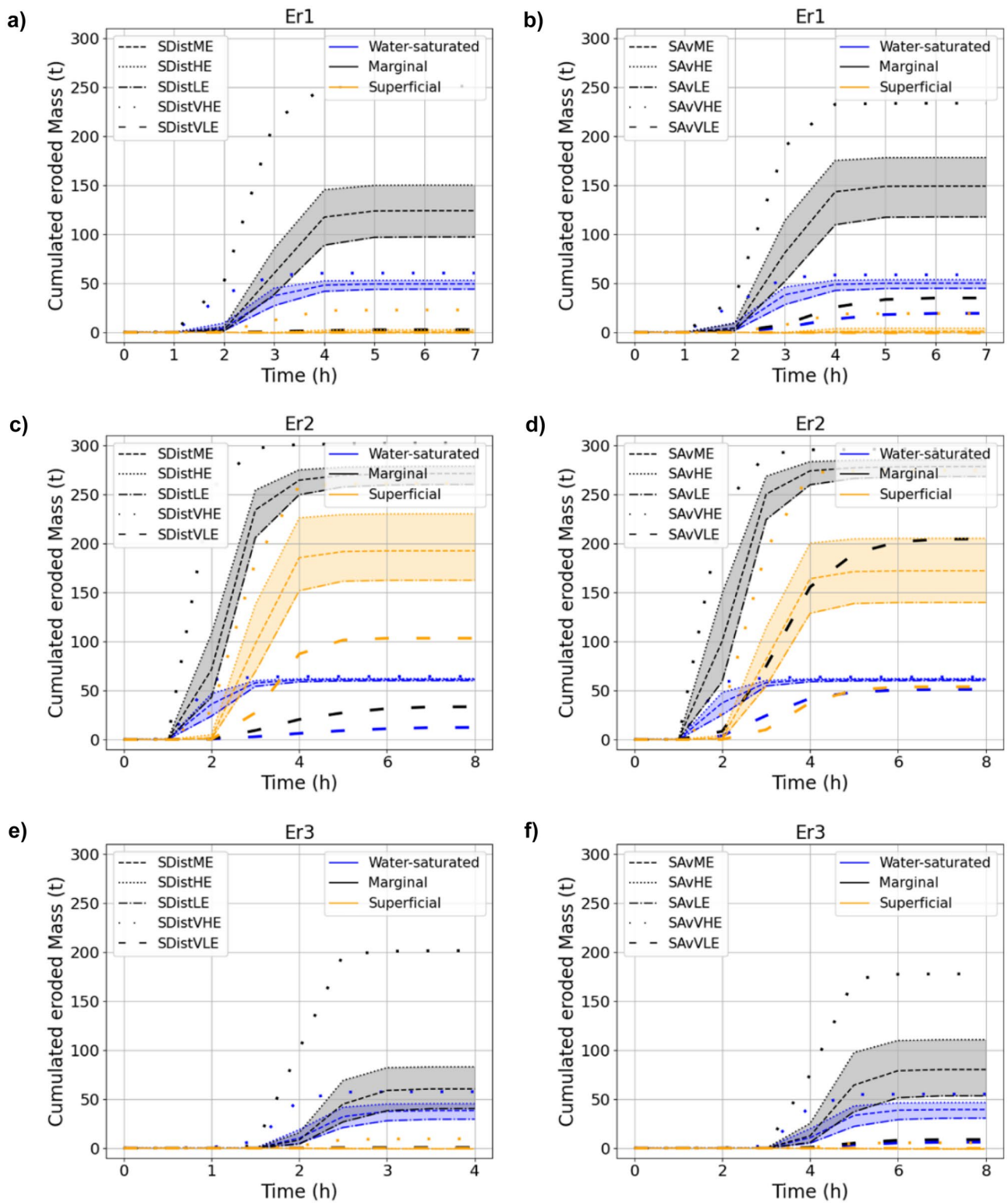


Fig. 9 Cumulated eroded masses for the three deposit zones (water-saturated, marginal, and superficial) for the spatially distributed (a, c, and e) and spatially averaged (b, d, and f) settings for the events Er1,

Er2, and Er3. The shaded areas represent the eroded masses between the 1st and the 3rd quartiles (between the low erodibility and the high erodibility scenarios)

Table 3 Eroded mass in each deposit zone for the spatially distributed and spatially averaged median settings (SDistME and SAVME)

Hydraulic scenario	Zone	Spatially distributed (SDist) setting		Spatially averaged (SAv) setting	
		Total eroded mass (t)	Eroded mass per area (kg m^{-2})	Total eroded mass (t)	Eroded mass per area (kg m^{-2})
<i>Er1</i>	Water-saturated	49	55	50	56
	Marginal	124	30	149	37
	Superficial	0.4	0.1	1.1	0.2
<i>Er2</i>	Water-saturated	61	68	61	68
	Marginal	271	66	279	68
	Superficial	193	39	172	35
<i>Er3</i>	Water-saturated	38	43	40	45
	Marginal	60	15	80	20
	Superficial	0	0	0	0

complete dataset, they could exceed 100% when the dataset was incomplete and when extreme values were used in the parametrization of the model. This shows that an area can contribute very differently if the erodibility variables are spatially distributed by zones or averaged.

3.3 Modeling assumptions and limitations

Very few or any numerical models deal with deposition of cohesive material in mountain rivers. Existing models focus on estuarine or reservoir environments (Sloff et al. 2013; Van Maren et al. 2015; Hoffman et al. 2017; Santoro et al. 2017) characterized mainly by low flow velocities and high-water depths. In these cases, the riverbed is composed of sand and mud. Due to a lack of measurements, several numerical works take into consideration the uncertainty due to the characterization of the cohesive sediments. To model the sediment transport in the Gironde Estuary, Orseau et al. (2021) conducted a sensitivity analysis on sediment variables. They showed that reducing the erosion critical shear stress by 20% leads to an increase of SSC by 73% and amplifies tidal variations. Allen et al. (2021) used Delft3D to simulate sediment transport in San Pablo Bay. Variation in sediment erodibility induced strong variations in erosion and deposition in the shallows system, but it caused no change in the total export from the shallows. In a lowland river, Chen et al. (2021) showed that the sediment conveyance was not sensitive to the cohesive sediment parameters. Hoffman et al. (2017) modeled reservoirs of the upper Rhine River with 1D sediment budget models. Based on a flume experiment, they assessed the uncertainty on critical shear stress and erosivity to be in the order of 50 and 100%, respectively. The model of the Iffezheim reservoir showed a high sensitivity to the Partheniades constant. The contrasted results of these previous works highlight the need to conduct specific sensitivity analysis depending on the environment and the objectives of the modeling approach.

To assess the uncertainty due to erodibility characterization, the present work relies on two main modeling simplifications and assumptions: (i) only one class of cohesive sediments was considered and (ii) the gravel bed was assumed to be stable. Several classes of sediments including the sand fraction could have been added in the model as in the previous work of Orseau et al. (2021). However, it would have added complexity to the model and the results would have been more difficult to analyze. It would also have required field measurements to assign specific erosion properties to each particle size class in the model. However, the available erodibility measurements corresponded to measurements of the overall behavior of the fine sediment matrix deposited in the river beds. Concerning the choice of a fixed bed in the model, it is obvious that it does not allow to represent the transport conditions for high flows, during which bedload can be a major component of the bed evolution in gravel-bed rivers. The contemporary numerical tools are now able to reproduce bed evolutions due to gravel movements. Cordier et al. (2016) succeeded in modeling with TELEMAC-2D the evolution of the Arc River in the Alps. Javernick et al. (2016), Williams et al. (2016), and Singh et al. (2017) simulated the evolution of braided rivers in New Zealand with Delft3D. Proceeding further along the spectrum, recent research works managed to include the effect of the vegetation on the evolution of gravel beds (Li et al. 2022). However, the actual work attended to simulate only the erosion of cohesive sediment deposited at the surface of gravel bars and not those contained in the gravel matrix. To this goal, the discharges of the simulated hydrological events were chosen to be lower than the gravel movement threshold. A prospect could be the simulation of the river reach evolution for a large range of discharges, from low flow to major floods, considering the three classes of sediments (cohesive, sand, and gravels). It would require a larger dataset to calibrate the bedload evolutions and the erosion of the fine sediments stored in the gravel bed matrix should be considered (Misset et al. 2021).

3.4 Recommendations to correctly parametrize the erodibility in numerical models

The analysis conducted in the three deposit zones (Section 3.2.2) showed that the water-saturated zone characteristics had a lower impact on the results than the marginal zone for the three modeled events. Indeed, interquartile differences were lower in the water-saturated zone compared to the marginal zone (Fig. 9). This is because during floods, hydraulic shear stresses were rapidly high in the water-saturated zone, leading to rapid erosion of sediments in this area. The median bed shear stress generated by the flow at $0.5 \text{ m}^3 \text{ s}^{-1}$ already exceeded the critical shear stress of the cohesive deposits in this area (Fig. 10). The marginal zone was the largest contributor to the SS flux. Figure 10 shows that the calculated bottom shear stress at $1 \text{ m}^3 \text{ s}^{-1}$ in the marginal zone exceeded the median of the critical shear stresses of the deposits. This explains the high sensitivity of this area to small floods, like Er3 with a $1 \text{ m}^3 \text{ s}^{-1}$ peak discharge, as shown in Fig. 9. The superficial zone characteristics had the largest impact on the results for high floods, because the critical shear stress of the sediments is near the median of the calculated shear stress for those floods. In view of the results, measurements in marginal and superficial zones should be preferred to measurements in the water-saturated zone. Furthermore, this latter zone has values of erodibility variables between those of the marginal and superficial zones (Fig. 5c, d). Therefore, it is not necessary to make measurements in this zone as it is possible to assign the average values of the marginal and superficial zones for the water-saturated zone. Given the reduced sensitivity of the model to the water-saturated zone, an error

on the erodibility values does not lead to high errors on the simulated eroded masses.

It is necessary to define the number of measurements needed to obtain a correct estimation of the distribution of the erodibility in the marginal and superficial zones. Since the erodibility measurements are time-consuming, the objective was to optimize the number of required measurements. The minimum number of measurements must contain almost all the information of the total sample, i.e., correct estimates of the statistics describing the distribution of the variables. The numerical results on the Galabre (Figs. 8 and 9) showed that the sensitivity of the modeled eroded mass was increased at the extremities of the distributions (i.e., below the 1st quartile and above the 3rd quartile) of the erodibility variables. As long as the model parameter values are between the 1st and 3rd quartile, the model prediction was good. The number of measurements performed must therefore correctly estimate at least the median, the 1st and 3rd quartiles, in the marginal and superficial zones. These three statistics will provide the ranges over which the variables have to be modified in the model as part of a sensitivity study.

For both variables (τ_{ce} and M) and both areas (marginal and superficial), the bootstrap sub-sampling methodology was adopted to estimate the minimal number of measurements required (Fig. 11). Results show that the larger the sample size, the better the estimation of the statistics was (median and quartiles). Indeed, the standard deviations (vertical bars) tended to decrease as the sample size increased, meaning that the statistical estimate was increasingly reliable as the sample size increased.

In the case of marginal deposits, five measurements (i.e., 10% of the total number of the campaign) were already sufficient to correctly estimate the three statistics of the critical

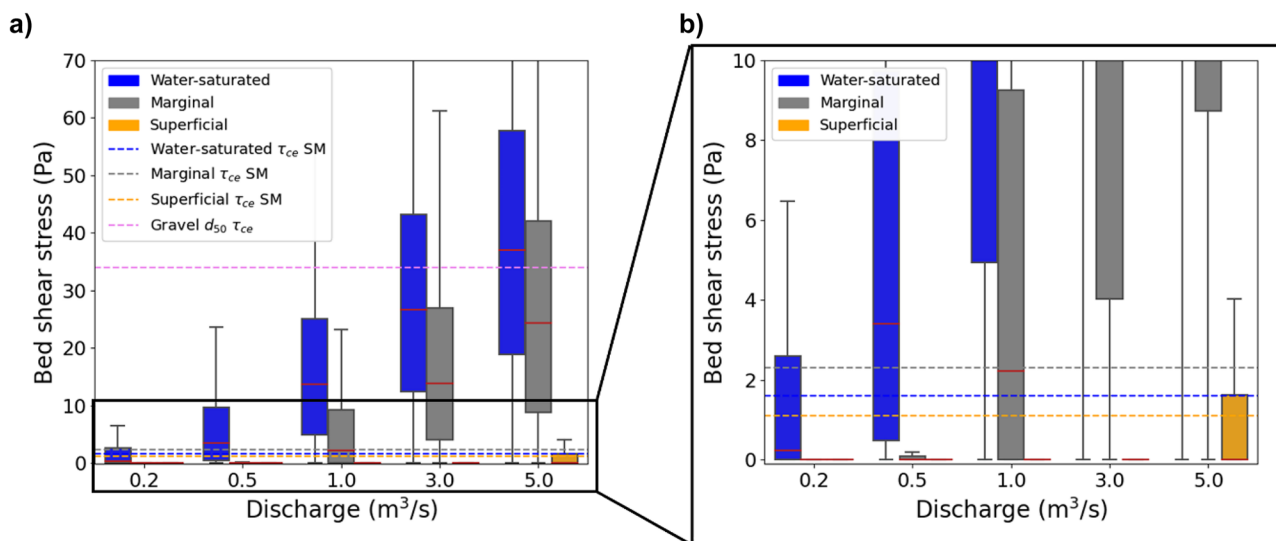


Fig. 10 Distribution of simulated bed shear stresses in the water-saturated, in the marginal, and in the superficial zone for different water discharges: 0.2, 0.5, 1, 3, and $5 \text{ m}^3 \text{ s}^{-1}$. In dotted lines: critical shear

stresses in each zone for the cohesive deposits for the SDistM scenario and for the median gravels

Marginal deposits

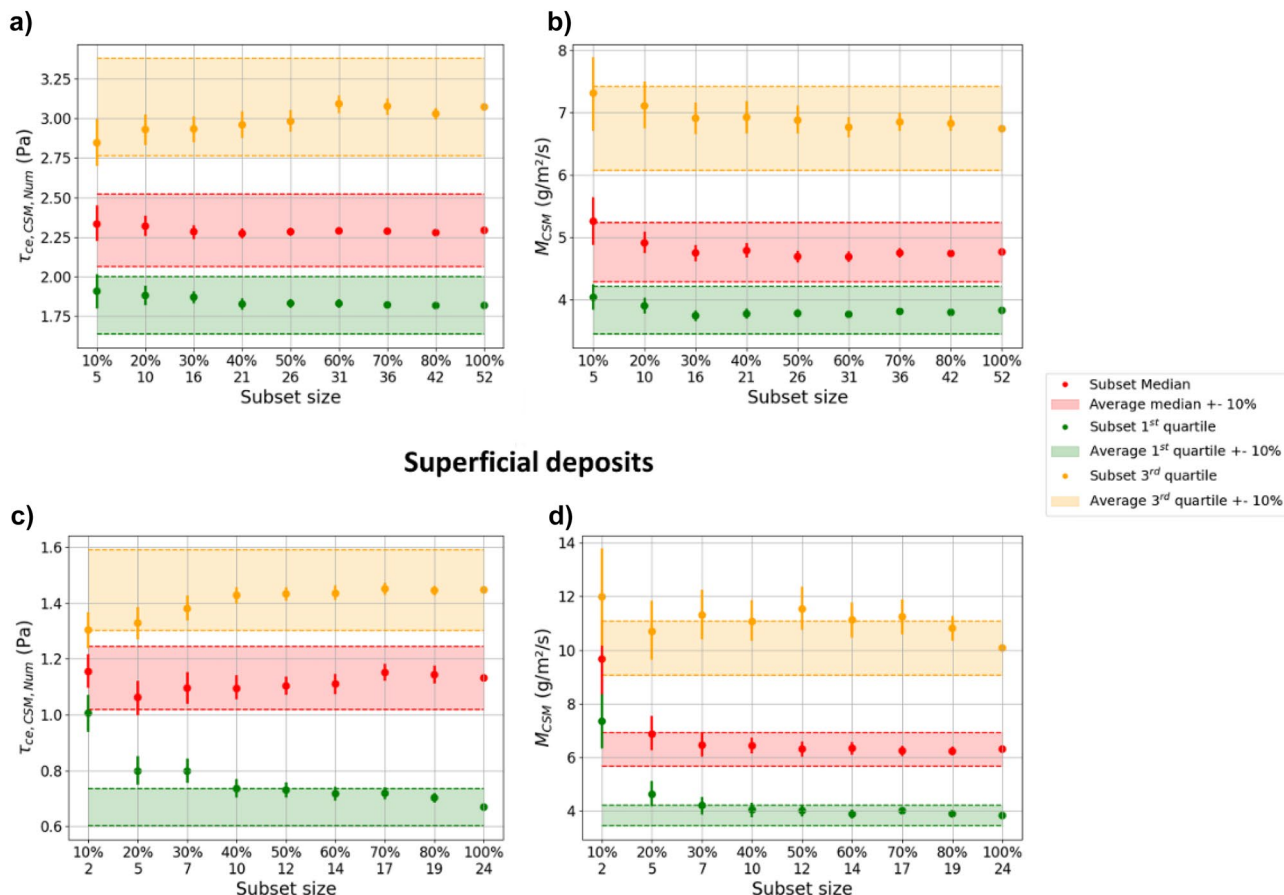


Fig. 11 Estimation of the median, the 1st, and the 3rd quartiles according to the sample size with the bootstrap methodology for both variables (τ_{ce} and M) in the marginal zone (a, b) and the superficial

zone (c, d). One hundred repeats for each subset were used for the estimation of the variable statistics

stress distribution with less than 10% deviation from the reference statistic (Fig. 11a). This was also true for the Partheniades constant (Fig. 11b), even though the values estimated with this sample for this variable were close to a 10% error. Nevertheless, we observed that for both variables, the statistics of interest quickly approached the statistic of the total sample with a lower uncertainty range (standard deviation). The statistics of these variables were thus very well estimated when the sample size was equal or larger than 16 measurements (i.e., 30% of the total sample).

Concerning the superficial deposits (Fig. 11c, d), the convergence of the statistics of interest was similar to the one in the marginal zone. For the critical shear stress, the median and the 3rd quartile were well estimated with only two measurements (10%), but it took at least between 10 (40%) and 17 measurements (70%) to correctly estimate the 1st quartile within a 10% error (Fig. 11c). For the M variable, the median and the 1st quartile were well estimated with seven measurements (30%), but the 3rd quartile was correctly estimated with

a sample between 14 (60%) and 19 (80%) measurements. This statistic slightly overestimated the desired value for this deposit zone (Fig. 11d). Thus, the variables in the superficial zone seemed more difficult to estimate than in the marginal zone and required more measurements. Although we cannot exclude that the variability of the sediments was greater in the superficial zone than in the marginal zone, part of this variability could come from the greater uncertainties of measurements with the CSM in the superficial zone. It is indeed more difficult to make measurements with the CSM when the deposits are too dry. Thus, this was reflected in the statistical distribution containing more variability for this zone.

4 Conclusions

The measurements evidenced that the spatial variability of the erodibility of cohesive sediments deposited in the Galabre river bed was controlled by the position and the height of the deposit

above the water level. Marginal deposits were the most resistant while superficial deposits were the least resistant, with water-saturated deposits in between.

A first numerical analysis was conducted on the sensitivity of simulated total eroded masses to this variability. The results showed that when the acquired dataset was robust and correctly estimated the variability, the total eroded mass had a low dependency on the variability of erodibility. An average value for the whole reach led to the same results as those obtained with specific erodibility values assigned in each deposition zone.

A second analysis was conducted on the sensitivity of masses eroded in each of the three zones to the spatial variability of the erodibility. Results showed that the differences between spatially distributed and spatially averaged erodibility settings were significant. Thus, if the objective of numerical modeling is to adequately reproduce the evolution of the deposits in each zone, it is necessary to use spatially distributed erodibility settings. However, if the dataset is incomplete and the measurements do not adequately capture the erodibility distribution, imposing different values of erodibility in the different zones could lead to more errors than an average erodibility setting on the whole reach.

From this analysis, we recommended focusing on marginal and superficial zones during field campaigns of erodibility measurements since these ones were the most contributory to the SS flux and have the larger impact on the model results. For the Galabre River, the August 2019 dataset shows that, to have a correct assessment, at least 10 to 15 measurements must be acquired in marginal zones and at least 15 to 20 in superficial zones.

This methodology was built on a large number of erodibility field measurements. Providing the availability of robust erodibility datasets, it can be generalized to other monitoring devices or other environments (e.g., reservoirs, estuaries, and lowland rivers). It may lead to an adaptation of monitoring strategies. The results underlined the relevance of using a field dataset to estimate both erodibility parameters in numerical models. The methodology allowed to define zones with distinct resistance to erosion and to assign specific values. This work opens new paths for calibration strategies that consider spatially distributed field information rather than finding the best parameters to fit the SSC data.

Supplementary Information The online version contains supplementary material available at <https://doi.org/10.1007/s11368-023-03438-6>.

Acknowledgements The authors would like to express special thanks to Ian G. Droppo for guidance during this work and for the provision of the CSM device and to G. Nord for providing data at the downstream station. The authors thank Guilhem Freche, Romain Biron, Catherine Coulaud, and Hervé Denis for field data collection at the Galabre site and Jacques Montariol for the help in the calibration of the numerical model. The authors thank the three anonymous reviewers and the guest editor for their helpful comments.

Funding This work was funded by the French National Association of Research and Technology (ANRT) and EDF R&D with the Industrial Conventions for Training through Research (CIFRE grant agreement 2018/1453). It was also supported by the French National Research Agency (ANR) under the grants ANR-18-CE01-0020 (DEAR project) and ANR-11-EQPX-0011 (EQUIPEX CRITEX project). This study was carried out in the Galabre site of the Draix-Bléone Observatory funded by INRAE, INSU, and OSUG and is part of OZCAR Research Infrastructure that is supported by the French Ministry of Research, French Research Institutions and Universities.

Data availability All observed data, numerical project and outputs are available upon request.

Declarations

Competing interests The authors declare no competing interests.

References

- Allen RM, Lacy JR, Stevens AW (2021) Cohesive sediment modeling in a shallow estuary: model and environmental implications of sediment parameter variation. *J Geoph Res Oceans* 126(9):e2021JC017219. <https://doi.org/10.1029/2021JC017219>
- Audouin Y, Benson T, Delinares M et al (2020) Introducing GAIA, the brand new sediment transport module of the TELEMAC-MASCARET system. In: XXVIth TELEMAC-MASCARET User Conference, 15 to 17 Oct 2019, Toulouse. <https://doi.org/10.5281/ZENODO.3611600>
- Bale AJ, Widdows J, Harris CB, Stephens JA (2006) Measurements of the critical erosion threshold of surface sediments along the Tamar Estuary using a mini-annular flume. *Cont Shelf Res* 26:1206–1216. <https://doi.org/10.1016/j.csr.2006.04.003>
- Brand A, Lacy JR, Gladding S et al (2015) Model-based interpretation of sediment concentration and vertical flux measurements in a shallow estuarine environment: shallow estuarine sediment dynamics. *Limnol Oceanogr* 60:463–481. <https://doi.org/10.1002/lno.10047>
- Camenen B, Jodeau M, Jaballah M (2013) Estimate of fine sediment deposit dynamics over a gravel bar using photography analysis. *Int J Sediment Res* 28:220–233. [https://doi.org/10.1016/S1001-6279\(13\)60033-5](https://doi.org/10.1016/S1001-6279(13)60033-5)
- Chen C-Y, Fytanidis DK, García MH (2021) Entrainment, transport, and fate of sediments during storm events in urban canals and rivers: case study on Bubbly Creek, Chicago. *J Hydraul Eng* 147:05021005. [https://doi.org/10.1061/\(ASCE\)HY.1943-7900.0001890](https://doi.org/10.1061/(ASCE)HY.1943-7900.0001890)
- Chou Y, Nelson KS, Holleman RC et al (2018) Three-dimensional modeling of fine sediment transport by waves and currents in a shallow estuary. *J Geoph Res Oceans* 123:4177–4199. <https://doi.org/10.1029/2017JC013064>
- Cordier F, Tassi P, Jodeau M, Camenen B (2016) Large-scale morphodynamics structures in the Arc en Maurienne River (France). In: Proc River Flow Conference, St Louis, Missouri, USA, July 2016, 1175–1183
- Dong H, Jia L, He Z et al (2020) Application of parameters and paradigms of the erosion and deposition for cohesive sediment transport modelling in the Lingdingyang Estuary, China. *Appl Ocean Res* 94:101999. <https://doi.org/10.1016/j.apor.2019.101999>
- Esteves M, Legout C, Navratil O, Evrard O (2019) Medium term high frequency observation of discharges and suspended sediment in a Mediterranean mountainous catchment. *J Hydrol* 568:562–574. <https://doi.org/10.1016/j.jhydrol.2018.10.066>
- Estrany J, Garcia C, Walling DE, Ferrer L (2011) Fluxes and storage of fine-grained sediment and associated contaminants in the Na

- Borges River (Mallorca, Spain). *Catena* 87:291–305. <https://doi.org/10.1016/j.catena.2011.06.009>
- Feng Z, Tan G, Xia J et al (2020) Two-dimensional numerical simulation of sediment transport using improved critical shear stress methods. *Int J Sediment Res* 35:15–26. <https://doi.org/10.1016/j.ijsrc.2019.10.003>
- Fryirs K (2013) (Dis)connectivity in catchment sediment cascades: a fresh look at the sediment delivery problem: (dis)connectivity in catchment sediment cascades. *Earth Surf Process Landf* 38:30–46. <https://doi.org/10.1002/esp.3242>
- Gaillardet J, Braud I, Hankard F et al (2018) OZCAR: the French network of critical zone observatories. *Vadose Zone J* 17:180067. <https://doi.org/10.2136/vzj2018.04.0067>
- Grabowski RC, Wharton G, Davies GR, Droppo IG (2012) Spatial and temporal variations in the erosion threshold of fine riverbed sediments. *J Soils Sediment* 12:1174–1188. <https://doi.org/10.1007/s11368-012-0534-9>
- Haddad H, Jodeau M, Legout C et al (2022) Spatial variability of the erodibility of fine sediments deposited in two alpine gravel-bed rivers: the Isère and Galabre. *Catena* 212:13. <https://doi.org/10.1016/j.catena.2022.106084>
- Harris RJ, Pilditch CA, Greenfield BL et al (2016) The influence of benthic macrofauna on the erodibility of intertidal sediments with varying mud content in three New Zealand estuaries. *Estuaries Coasts* 39:815–828. <https://doi.org/10.1007/s12237-015-0036-2>
- Hervouet J-M (2007) *Hydrodynamics of free surface flows: modelling with the finite element method*. John Wiley & Sons, Chichester, UK
- Hodgkins R, Cooper R, Wadham J, Tranter M (2003) Suspended sediment fluxes in a high-Arctic glacierised catchment: implications for fluvial sediment storage. *Sediment Geol* 162:105–117. [https://doi.org/10.1016/S0037-0738\(03\)00218-5](https://doi.org/10.1016/S0037-0738(03)00218-5)
- Hoffman E, Lyons J, Boxall J et al (2017) Spatiotemporal assessment (quarter century) of pulp mill metal (loid) contaminated sediment to inform remediation decisions. *Environ Monit Assess* 189(6):1–17. <https://doi.org/10.1007/s10661-017-5952-0>
- Javernick L, Hicks DM, Measures R, Caruso B, Brasington J (2016) Numerical modelling of braided rivers with structure-from-motion-derived terrain models. *River Res Appl* 32(5):1071–1081. <https://doi.org/10.1002/rra.2918>
- Joensuu M, Pilditch CA, Harris R et al (2018) Sediment properties, biota, and local habitat structure explain variation in the erodibility of coastal sediments: variation in the erodibility of coastal sediments. *Limnol Oceanogr* 63:173–186. <https://doi.org/10.1002/lno.10622>
- Kemp P, Sear D, Collins A et al (2011) The impacts of fine sediment on riverine fish. *Hydrol Process* 25:1800–1821. <https://doi.org/10.1002/hyp.7940>
- Kondolf GM, Gao Y, Annandale GW et al (2014) Sustainable sediment management in reservoirs and regulated rivers: experiences from five continents. *Earth's Future* 2:256–280. <https://doi.org/10.1002/2013EF000184>
- Krone RB (1962) *Flume studies of transport of sediment in estuarial shoaling processes*. Final Report, Hydr Engr. and Samitary Engr. Res. Lab., Univ. of California
- Legout C, Droppo IG, Coutaz J et al (2018) Assessment of erosion and settling properties of fine sediments stored in cobble bed rivers: the Arc and Isère alpine rivers before and after reservoir flushing: erosion and settling dynamics of fine sediments in cobble bed rivers. *Earth Surf Process Landf* 43:1295–1309. <https://doi.org/10.1002/esp.4314>
- Legout C, Freche G, Biron R et al (2021) A critical zone observatory dedicated to suspended sediment transport: the meso-scale Galabre catchment (southern French Alps). *Hydrol Process* 35(3):e14084. <https://doi.org/10.1002/hyp.14084>
- Li J, Claude N, Tassi P et al (2022) Effects of vegetation patch patterns on channel morphology: a numerical study. *J Geophys Res Earth Surf* e2021JF006529. <https://doi.org/10.1029/2021JF006529>
- Lopes JF, Dias JM, Dekeyser I (2006) Numerical modelling of cohesive sediments transport in the Ria de Aveiro lagoon, Portugal. *J Hydrol* 319:176–198. <https://doi.org/10.1016/j.jhydrol.2005.07.019>
- Lumborg U, Andersen TJ, Pejrup M (2006) The effect of Hydrobia ulvae and microphytobenthos on cohesive sediment dynamics on an intertidal mudflat described by means of numerical modelling. *Estuar Coast Shelf Sci* 68(1–2):208–220. <https://doi.org/10.1016/j.ecss.2005.11.039>
- Mathers KL, Collins AL, England J et al (2017) The fine sediment conundrum; quantifying, mitigating and managing the issues. *River Res Appl* 33:1509–1514. <https://doi.org/10.1002/rra.3228>
- Misset C, Recking A, Legout C et al (2019) An attempt to link suspended load hysteresis patterns and sediment sources configuration in alpine catchments. *J Hydrol* 576:72–84. <https://doi.org/10.1016/j.jhydrol.2019.06.039>
- Misset C, Recking A, Legout C et al (2021) Assessment of fine sediment river bed stocks in seven Alpine catchments. *Catena* 196:104916. <https://doi.org/10.1016/j.catena.2020.104916>
- Navratil O, Esteves M, Legout C et al (2011) Global uncertainty analysis of suspended sediment monitoring using turbidimeter in a small mountainous river catchment. *J Hydrol* 398:246–259. <https://doi.org/10.1016/j.jhydrol.2010.12.025>
- Navratil O, Legout C, Gateuille D et al (2010) Assessment of intermediate fine sediment storage in a braided river reach (southern French Prealps). *Hydrol Process* 24(10):1318–1332. <https://doi.org/10.1002/hyp.7594>
- Nord G, Michielin Y, Biron R et al (2020) An autonomous low-power instrument platform for monitoring water and solid discharges in mesoscale rivers. *Geosci Instrum Methods Data Syst* 9:41–67. <https://doi.org/10.5194/gi-9-41-2020>
- Orseau S, Huybrechts N, Tassi P et al (2021) Two-dimensional modeling of fine sediment transport with mixed sediment and consolidation: application to the Gironde Estuary, France. *Int J Sediment Res* 36:736–746. <https://doi.org/10.1016/j.ijsrc.2019.12.005>
- Orwin JF, Smart CC (2004) Short-term spatial and temporal patterns of suspended sediment transfer in proglacial channels, small River Glacier, Canada. *Hydrol Process* 18:1521–1542. <https://doi.org/10.1002/hyp.1402>
- Park J, Hunt JR (2017) Coupling fine particle and bedload transport in gravel-bedded streams. *J Hydrol* 552:532–543. <https://doi.org/10.1016/j.jhydrol.2017.07.023>
- Partheniades E (1965) Erosion and deposition of cohesive soils. *J Hydrol Div* 91(1):105–139
- Santoro P, Fossati M, Tassi P et al (2017) A coupled wave–current–sediment transport model for an estuarine system: application to the Río de la Plata and Montevideo Bay. *Appl Math Model* 52:107–130. <https://doi.org/10.1016/j.apm.2017.07.004>
- Singh U, Crosato A, Giri S, Hicks M (2017) Sediment heterogeneity and mobility in the morphodynamic modelling of gravel-bed braided rivers. *Adv Water Resour* 104:127–144. <https://doi.org/10.1016/j.advwatres.2017.02.005>
- Sloff K, van Spijk A, Stouthamer E, Sieben A (2013) Understanding and managing the morphology of branches incising into sand-clay deposits in the Dutch Rhine Delta. *Int J Sediment Res* 28(2):127–138. [https://doi.org/10.1016/S1001-6279\(13\)60025-6](https://doi.org/10.1016/S1001-6279(13)60025-6)
- Syvitski JPM (2005) Impact of humans on the flux of terrestrial sediment to the global coastal ocean. *Science* 308:376–380. <https://doi.org/10.1126/science.1109454>
- Syvitski JPM, Peckham SD, Hilberman R, Mulder T (2003) Predicting the terrestrial flux of sediment to the global ocean: a planetary perspective. *Sediment Geol* 162:5–24. [https://doi.org/10.1016/S0037-0738\(03\)00232-X](https://doi.org/10.1016/S0037-0738(03)00232-X)

- Tassi P, Benson T, Delinares M et al (2023) GAIA—a unified framework for sediment transport and bed evolution in rivers, coastal seas and transitional waters in the TELEMAC-MASCARET modelling system. *Environ Model Softw* 159:105544. <https://doi.org/10.1016/j.envsoft.2022.105544>
- Tolhurst TJ, Black KS, Shayler SA et al (1999) Measuring the in situ erosion shear stress of intertidal sediments with the cohesive strength meter (CSM). *Estuar Coast Shelf Sci* 49:281–294. <https://doi.org/10.1006/ecss.1999.0512>
- Tolhurst TJ, Defew EC, de Brouwer JFC et al (2006) Small-scale temporal and spatial variability in the erosion threshold and properties of cohesive intertidal sediments. *Cont Shelf Res* 26:351–362. <https://doi.org/10.1016/j.csr.2005.11.007>
- Van Maren DS, van Kessel T, Cronin K, Sittoni L (2015) The impact of channel deepening and dredging on estuarine sediment concentration. *Cont Shelf Res* 95:1–14. <https://doi.org/10.1016/j.csr.2014.12.010>
- Walling DE, Owens PN, Carter J et al (2003) Storage of sediment-associated nutrients and contaminants in river channel and floodplain systems. *Appl Geochem* 18:195–220. [https://doi.org/10.1016/S0883-2927\(02\)00121-X](https://doi.org/10.1016/S0883-2927(02)00121-X)
- Widdows J, Friend PL, Bale AJ et al (2007) Inter-comparison between five devices for determining erodability of intertidal sediments. *Cont Shelf Res* 27:1174–1189. <https://doi.org/10.1016/j.csr.2005.10.006>
- Wilkes MA, Gittins JR, Mathers KL et al (2018) Physical and biological controls on fine sediment transport and storage in rivers. *Wiley Interdiscip Rev Water* 6(2):e1331. <https://doi.org/10.1002/wat2.1331>
- Williams RD, Measures R, Hicks DM, Brasington J (2016) Assessment of a numerical model to reproduce event-scale erosion and deposition distributions in a braided river. *Water Resour Res* 52(8):6621–6642. <https://doi.org/10.1002/2015WR018491>
- Wood PJ, Armitage PD (1999) Sediment deposition in a small lowland stream - management implications. *Reg Rivers Res Manag Int J Devoted River Res Manag* 15(1–3):199–210

Publisher's Note Springer Nature remains neutral with regard to jurisdictional claims in published maps and institutional affiliations.

Springer Nature or its licensor (e.g. a society or other partner) holds exclusive rights to this article under a publishing agreement with the author(s) or other rightsholder(s); author self-archiving of the accepted manuscript version of this article is solely governed by the terms of such publishing agreement and applicable law.